

Effect of nickel in solid solution on hydrogen transport kinetics in low alloy steels

Hans Husby¹, Afrooz Barnoush², Mariano Iannuzzi³, Roy Johnsen⁴

¹ NTNU*, 7491 Trondheim, Norway, hans.husby@ntnu.no

² NTNU, 7491 Trondheim, Norway, afrooz.barnoush@ntnu.no

³ GE Oil & Gas and NTNU, 1338 Sandvika, Norway, mariano.iannuzzi@ntnu.no

⁴ NTNU, 7491 Trondheim, Norway, roy.johnsen@ntnu.no

Abstract: The use of low alloy steels (LAS) in H₂S-containing environments in the oil and gas industry is governed by the ISO standard 15156-2 (NACE MR0175-2). One requirement, which has been disputed over the years, is that the nickel (Ni) content shall not exceed 1 wt%. This work investigated the effect of Ni in solid solution on hydrogen diffusion, solubility, and trapping in ferritic/pearlitic research-grade LAS with nominal Ni contents from 0 to 3 wt%. Hydrogen permeability experiments were carried out in a Devanathan-Stachurski setup at 15, 45 and 70 °C. The effective diffusion coefficients, calculated by the t_{lag} method, decreased with increasing Ni content. The sub-surface hydrogen concentration in lattice and trap sites increased with increasing Ni content. There was no difference between the first and subsequent hydrogen permeation transients, suggesting that Ni in solid solution forms reversible traps. The effect of Ni in refining the microstructure may be superimposed on the effect of Ni in solid solution, and should be investigated in future work.

Keywords: Nickel; low alloy steel; hydrogen; permeability; oil & gas

Introduction

Low alloy steels (LAS) are widely used in the oil and gas industry. In H₂S-containing environments, the use of LAS is governed by ISO standard 15156-2 [1] (NACE MR0175-2). The standard limits the nickel (Ni) content to maximum 1 wt%, due to concerns regarding sulfide stress cracking (SSC) resistance. Despite extensive investigations in the 1980's, the engineering community has yet to reach consensus as to whether the cap on Ni is scientifically justified. Ni improves LAS hardenability and lowers the ductile to brittle transition temperature with a moderate penalty on weldability. Qualifying LAS with Ni contents above 1 wt% would be a technology enabler in developing sour reservoirs with severe temperature and pressure conditions. [2]

Hydrogen uptake, diffusion, and trapping are properties that influence the metals' resistance to hydrogen stress cracking (HSC) (SSC is a form of HSC in the presence of H₂S [3]). Ni affects these properties, both as an element in solid solution and due to its refining effect on the microstructure.

Yoshino and Minozaki [4], Asahi and Ueno [5], Yamane et al. [6] and Wilde et al. [7] investigated hydrogen permeability of quenched and tempered (QT) steels with varying Ni

* Norwegian University of Science and Technology

contents exposed to different environments. The effective diffusion coefficient generally decreased with increasing Ni content. Results were not consistent with the effect of Ni on hydrogen solubility and steady state permeation flux. The effect of Ni in solid solution in the ferrite phase cannot be determined from the results on QT steels.

Beck et al. [8] investigated hydrogen diffusion and solubility as a function of Ni content in pure Fe-Ni alloys using a permeation technique at temperatures from 27 to 90 °C. The authors assumed purely ferritic microstructures up to 8 wt% Ni. They reported a decrease in the effective hydrogen diffusion coefficient and an increase in hydrogen solubility with increasing Ni content. Dresler and Frohberg [9] criticized that the metallurgical treatment was not precisely stated in the work of Beck et al., and Yamanishi et al. [10] questioned whether the microstructures were actually entirely ferritic. Dresler and Frohberg carried out diffusion experiments at 25 °C on Fe-Ni alloys, which according to the authors, had a body-centered cubic (bcc) microstructure up to 5 at% (~5 wt%) Ni. The diffusion coefficient decreased slightly with increasing Ni content up to 5 at%, with the largest reduction between 0.04 to 0.15 at% Ni. Hydrogen solubilities were not estimated. Neither of these three works investigated irreversible vs. reversible trapping by performing consecutive charging transients.

The objective of this work was to investigate the effect of solid solution Ni on hydrogen diffusion, solubility and trapping in the ferrite phase, using ferritic/pearlitic research-grade LAS with nominal Ni contents from 0 to 3 wt% specifically manufactured for this project.

Experimental

Materials

Four research grade LAS with nominal Ni contents from 0 to 3 wt% were produced. The actual chemical compositions are given in Table 1. Impurity levels were analyzed using glow discharge mass spectroscopy, and the susceptibility to temper embrittlement was quantified by calculating the X (Bruscatto) and J (Watanabe) factors [11]. The highest X-factor was 0.6, and the highest J-factor was 9.1, suggesting all alloys can be considered immune to temper embrittlement [12].

Table 1. Chemical compositions of research grade LAS, analyzed by methods specified in ASTM E1019-11/CO [13] and ASTM E1479-99/CTP3101/ICP [14]. Iron (Fe) balances to 100 wt%.

Alloy	Ni [wt%]	Mn [wt%]	Si [wt%]	C [wt%]
0 wt% Ni	0.00	1.30	0.24	0.17
1 wt% Ni	0.97	1.30	0.24	0.17
2 wt% Ni	1.85	1.28	0.23	0.17
3 wt% Ni	2.86	1.30	0.24	0.17

The materials were cast and hot-rolled at the supplier and delivered as plates with thicknesses of about 1 cm. Samples for the permeability experiments were made using electrical discharge

machining (EDM). The disks in the experiments had a diameter of 29 mm and a thickness of about 1.15 mm after grinding.

The materials had a banded microstructure in the as-received condition. Therefore, samples were homogenized by heat-treating at 1200 °C for seven days. The samples were encapsulated in quartz glass with vacuum to avoid oxidation and decarburization. After 7 days at 1200 °C, the samples were oven cooled to 500 °C (i.e. below the A_1 temperature) followed by heating to 930 °C (i.e. above the A_3 temperature), repeated twice. Subsequently, the samples were oven cooled to 500 °C and, finally, air cooled to room temperature. The goal was to refine the microstructures after the long-lasting homogenization. Oven cooling rates ranged from approximately 7 °C min⁻¹ at 930 °C to roughly 1 °C min⁻¹ at 600 °C. Since Ni refines the microstructure [15], an additional heating step was applied to the 2 and 3 wt% Ni samples to obtain comparable microstructures for all Ni contents. After a third austenitization at 930 °C, the 2 and 3 wt% Ni samples were not oven cooled, but rather cooled at a fixed cooling rate of 1.5 °C min⁻¹, i.e. a cooling rate about 5 times slower than that obtained by oven cooling, down to 600 °C before air cooling to room temperature. Figure 1 illustrates the heat treatment processes.

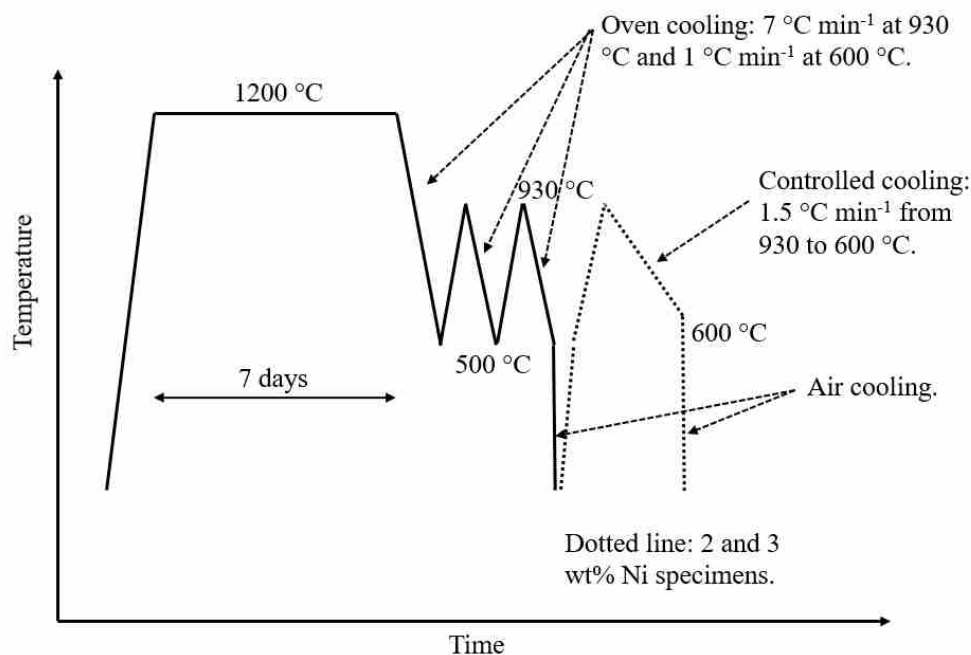


Figure 1. Illustration of the heat treatment process. The solid temperature-time line was followed for all samples from 0 to 3 wt% Ni, while the dashed line was followed for the 2 and 3 wt% Ni samples.

The microstructures of all samples were characterized using scanning electron microscopy (SEM). The samples were first ground to U.S. grit 600 (European P1200) for the permeability experiments and posteriorly polished using a diamond suspension down to 1 μm particle size, before they were electropolished to reveal the microstructures. Secondary electron images were captured using a commercially available SEM with a beam energy of 15 kV.

Hydrogen permeability experiments

Permeability experiments were carried out on the samples in Table 1 at 15, 45 and 70 °C \pm 1 °C. For each Ni content, the same sample was used at all temperatures, starting with the lowest temperature. Three charge/discharge transients were performed at each temperature.

The permeability experiments were carried out in a Devanathan-Stachurski setup. Two standards, ISO 17081 [16] and ASTM G148-97 [17], give guidelines on how to execute such experiments and how to analyze the data. Electrochemical permeability experiments are executed with two individual electrochemical cells that are separated by the sample of interest. On one side, hydrogen is charged into the material by applying a cathodic current. Hydrogen absorbs into the material and diffuses through the sample due to a concentration gradient. On the other side, an anodic potential is applied to the sample. The hydrogen atoms are oxidized back to H⁺, and the oxidation current (called permeation current) is measured. The permeation current can change with time and from the first to the subsequent charging transients due to hydrogen trapping effects. Hydrogen solubility, effective diffusivity, and reversible and irreversible trapping can be evaluated as described later.

The samples were ground on both sides to US grit 600 (European P1200) as recommended in ASTM G148-97 [17]. The samples were rinsed in ethanol, put in an ultrasonic bath, and then dried. Sample thickness was measured at five evenly distributed locations around the circumference, and the average value was used as sample thickness. The thicknesses of the samples in the tests were around 1.15 mm. The exposed radius of the disk was 12.45 mm. This gives a radius-to-thickness ratio of about 10:1 as recommended in ISO 17081 [16], and shall ensure that permeation analysis is based on one-dimensional diffusion.

Figure 2 shows the experimental cell used for the experiments. Two individual cells were clamped together with the sample sitting in between. The system was sealed by rubber O-rings on both sides of the sample towards the glass walls. The white polymer ring worked as a support to keep the setup in place and ensure reproducible mounting. A pin provided electrical connection to the sample. Each compartment had a volume of about 98 cm³, hence satisfying the recommendation in ASTM G148-97 [17] of a solution volume to metal area ratio greater than 20 ml cm⁻².

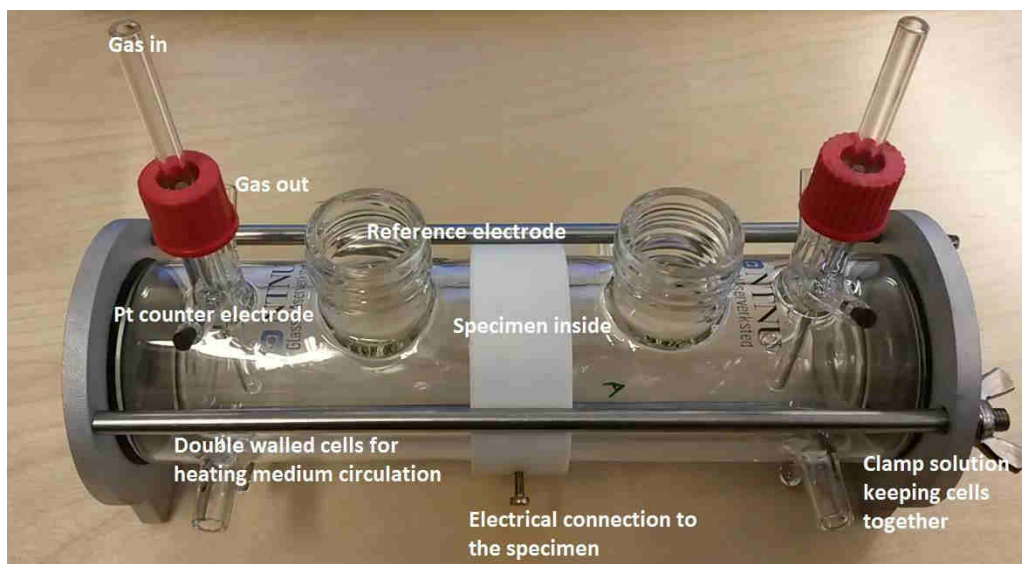


Figure 2. Image of electrochemical permeability cell.

Water with controlled temperature circulated through the outer walls of the glass cells. Nitrogen gas (5.0 instrumental quality, 99.999 % pure) was bubbled in both compartments before and during the experiments to avoid oxygen contamination. Luggin capillaries with reference electrodes were inserted into the large openings on both sides seen in Figure 2. The reference electrodes were mercury-mercurous electrodes ($\text{Hg}/\text{Hg}_2\text{SO}_4/\text{SO}_4^{2-}$ in saturated K_2SO_4 solution) with potentials +0.41 V vs. saturated Calomel electrode (SCE) and +0.65 V vs. standard hydrogen electrode (SHE) [18]. All potentials written in this article are in the mercury-mercurous scale (MME). The reference electrodes were placed in the Luggin capillaries filled with a borax solution, described below. Platinum foil was used as counter electrodes. The electrochemistry was controlled using two potentiostats.

In both compartments, the electrolyte was a mix of glycerin/glycerol, borax (di-Sodium tetraborate decahydrate) and distilled water. The solution was prepared by mixing 620 grams borax powder with glycerin to a total of 1 liter solution. The borax/glycerin was then mixed with distilled water to a volumetric 80/20 ratio. Prior to experiments, the pH was about 7 and the electrical resistivity was approximately $450 \Omega \text{ cm}$. Because LAS remain passive in the borax solution, a palladium coating was not applied on either side. The potential on the anodic side during permeability experiments was 0 V_{MME} . The cathodic side was polarized to 0 V_{MME} during hydrogen discharge. A fixed cathodic current density of $45 \mu\text{A cm}^{-2}$ was applied to the cathodic side during hydrogen charging. The selections of anodic potential and cathodic charging current are discussed later. A stable background current was obtained before all charging transients.

Electrochemical polarization experiments

Polarization curves were obtained in the borax electrolyte to determine the anodic potential and the cathodic charging current density for the permeability tests. 0 and 3 wt% Ni samples were tested at 15 and 70 °C. Before polarization, samples remained at the open circuit potential (OCP) for 1 hour with continuous nitrogen bubbling to remove oxygen. The cathodic current

density at which hydrogen bubbles formed was visually determined during polarization from OCP in the cathodic direction at 0.2 mV s⁻¹ (12 mV min⁻¹). A full polarization curve was recorded from -1.6 to 1.2 V_{MME} with a scan rate of 0.2 mV s⁻¹. As-received samples were used for the polarization curves. The surfaces were prepared following the procedure described for the permeability samples.

Analysis of the results

The sub-surface hydrogen concentration at lattice sites in the material, C₀ in mol m⁻³, can be calculated from Equation (1) [16]. The sub-surface lattice hydrogen concentration is a direct consequence of the severity of the environment [19].

$$J_{ss} = \frac{I_{ss}}{F A} = \frac{D_l C_0}{L} \quad (1)$$

J_{ss} is the steady-state hydrogen permeation flux in mol m⁻² s⁻¹. I_{ss} is the corresponding steady-state current in Ampere. J_{ss} is independent of trapping [20]. A is the exposed area in m². D_l is the ideal lattice diffusion coefficient in m² s⁻¹. As long as the metal is not highly alloyed [17], or no longer has a bcc structure [21], D_l is independent of metallurgical treatment and alloying, and can be considered to be the same as for pure annealed iron [21]. The lattice diffusion coefficient is defined by Equation (2) [19].

$$D_l = D_0 \exp\left(\frac{-E_l}{R T}\right) \quad (2)$$

Where D₀ is the frequency factor in m² s⁻¹, E_l is the activation energy for jumps between interstitial lattice sites in J mol⁻¹, R is the gas constant in J mol⁻¹ K⁻¹ and T is the temperature in Kelvin [19]. From ambient temperature and up to 80 °C, when the preferred trapping site in bcc iron is tetrahedral interstitial, values for D₀ and E_l of 7.23 10⁻⁸ m² s⁻¹ and 5.69 kJ mol⁻¹, respectively, can be used [19].

If only reversible trapping is important and the trap occupancy is low during a permeability experiment, so that the permeation transient is described by Fick's law, the sub-surface concentration of hydrogen atoms in lattice and reversible trap sites, C_{OR} in mol m⁻³, can be approximated by Equation (3) [17, 19].

$$J_{ss} = \frac{D_{eff} C_{OR}}{L} \quad (3)$$

D_{eff} is the effective diffusion coefficient describing the permeation transient in m² s⁻¹, and L is the sample thickness in meters. One of three methods suggested in ISO 17081 [16] can be used to determine D_{eff}. The t_{lag} method defines the effective diffusion coefficient from the time (t_{lag} in seconds) it takes to reach J(t) J_{ss}⁻¹ = 0.63, and is calculated from equation (4).

$$D_{eff} = \frac{L^2}{6 t_{lag}} \quad (4)$$

With only reversible trapping and low trap occupancy, it is possible to estimate the trap density, N_r in sites m^{-3} , and trap strength, E_b in $J mol^{-1}$, using Equation (5) [22].

$$D_{eff} = \frac{D_0 \exp\left(\frac{-E_l}{RT}\right)}{1 + \frac{N_r}{N_l} \exp\left(\frac{-E_b}{RT}\right)} \quad (5)$$

N_l is the density of lattice sites in sites m^{-3} [22]. At high temperature, the second term in the denominator will decrease towards zero and lattice diffusion will dominate [22]. At low temperature, the second term in the denominator will dominate and trapping becomes the main factor [22]. In this situation, for metals with only one type of reversible trap sites, D_{eff} can be described by Equation (6) [23, 24].

$$D_{eff} = D_0 \frac{N_l}{N_r} \exp\left(\frac{-(E_b + E_l)}{RT}\right) \quad (6)$$

If D_{eff} is measured at different temperatures, a plot of the value on a logarithmic scale against the inverse of the temperature should make a straight line with the expression $D_{eff} = A \exp(-B (RT)^{-1})$ [24]. Constants A and B are obtained from the plot, and Equations (7) and (8) can be used to calculate the number and strength of traps [24]. A value of N_l of $5.2 \cdot 10^{23}$ sites cm^{-3} has been used in literature at ambient temperatures [20].

$$N_r = \frac{D_0 N_l}{A} \quad (7)$$

$$E_b = B - E_l \quad (8)$$

Low occupancy of trap sites corresponds to low lattice sub-surface hydrogen concentrations; lower than those measured for steel in acidified H_2S solutions [20]. If trap occupancy is not low, the permeation transient cannot be described by a single effective diffusion coefficient [19]. D_{eff} will constantly change during the permeation transient, and its value will depend on which part of the curve is used for the fit [19]. Another complicating factor is that D_{eff} is a function of the hydrogen content due to a concentration dependency on trap occupancy [25]. Despite the limitations, it can be pragmatically useful to calculate D_{eff} based on the t_{lag} method [26] e.g. to compare material variables under the same environmental severity [20].

Results

Material characterization

All the tested samples had ferritic/pearlitic microstructures. The grain size decreased from 0 to 1 wt% Ni and from 2 to 3 wt% Ni. The fraction of pearlite increased with increasing Ni content (the 0 wt% Ni sample could have become slightly decarburized during the heat treatment). SEM micrographs obtained from electropolished surfaces are shown in Figure 3.

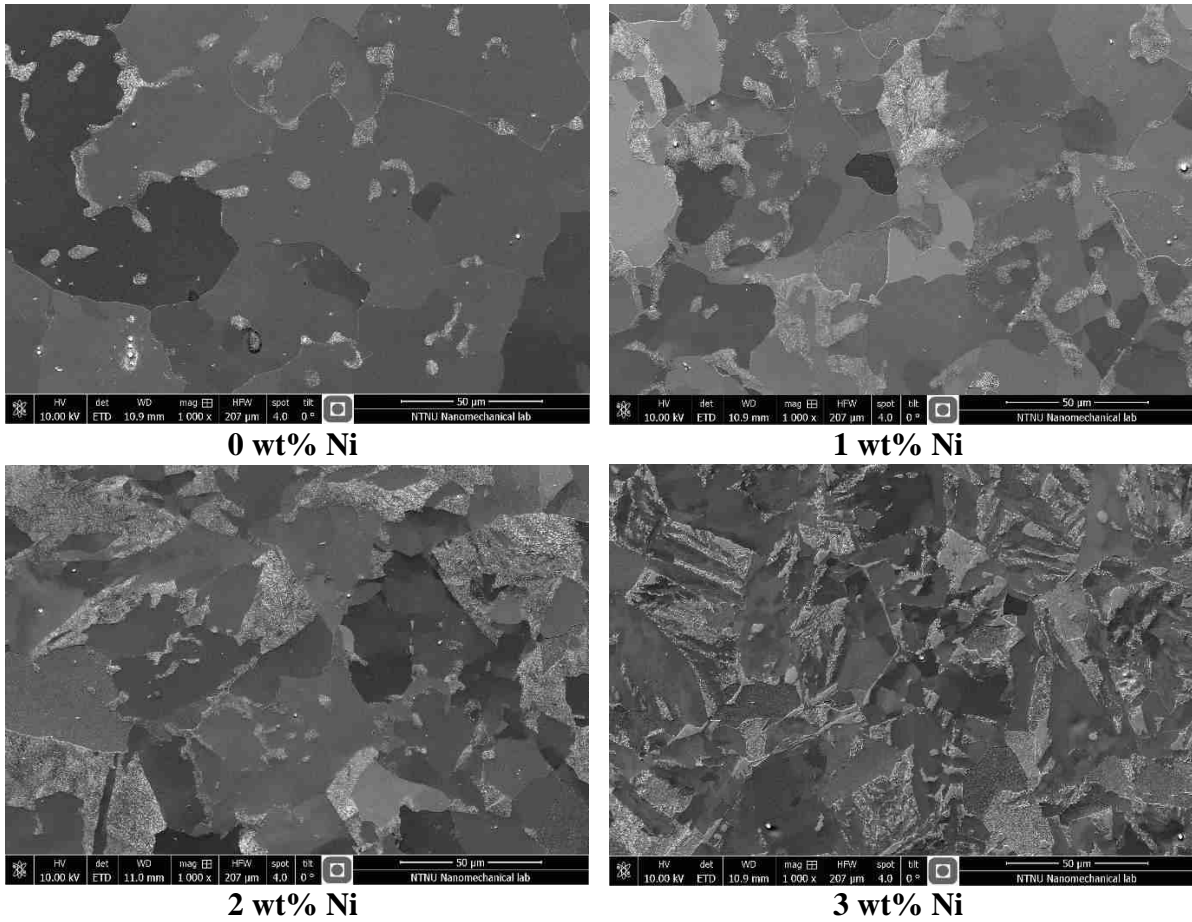


Figure 3. SEM micrographs of samples from the permeability experiments. Microstructures were revealed by electro polishing.

Electrochemical polarization experiments

Polarization curves of 0 and 3 wt% Ni samples in the borax solution at 15 and 70 °C are presented in Figure 4. The materials had an active-passive behavior in the borax solution, similar to that of stainless steels in reducing acids.

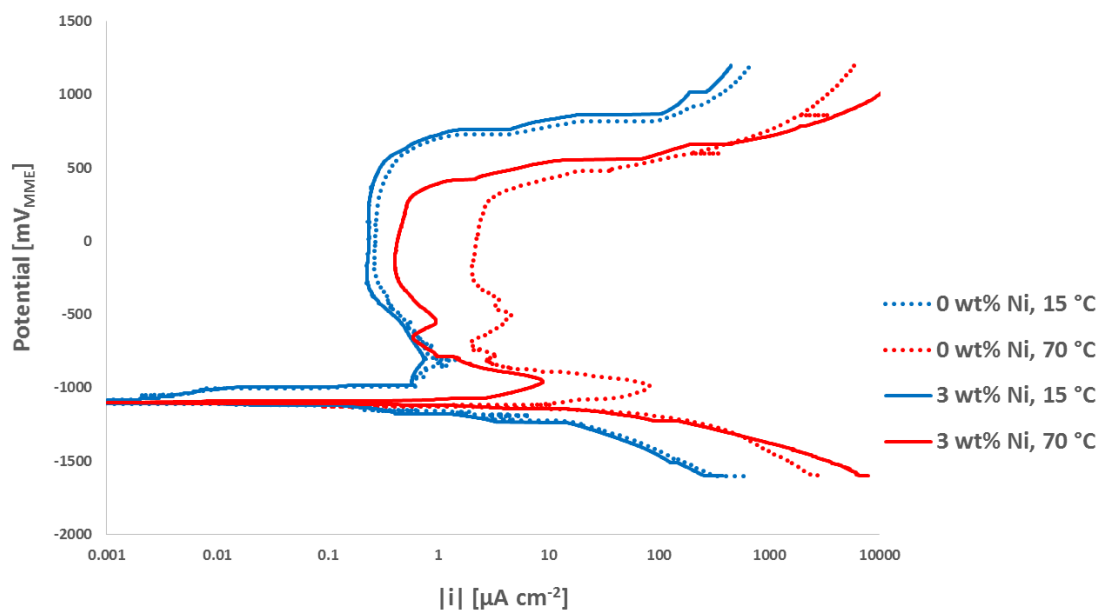


Figure 4. Polarization curves of 0 and 3 wt% Ni samples at 15 and 70 °C in borax solution, recorded with scan rates of 0.2 mV s^{-1} .

Table 2 lists some key values obtained from the polarization curves. The passive potential region was smaller, and the passive current density was higher, at 70 °C than at 15 °C. The 3 wt% Ni sample had a lower corrosion current density than the 0 wt% Ni sample at both 15 and 70 °C.

Table 2. Key values obtained from the polarization curves of 0 and 3 wt% Ni samples in borax solution at 15 and 70 °C.

	15 °C		70 °C	
	0 wt% Ni	3 wt% Ni	0 wt% Ni	3 wt% Ni
E_{OCP} [mV _{MME}]	-1100	-1100	-1100	-1100
E_{Flade} [mV _{MME}]	-812	-739	-993	-962
$E_{\text{pitting/transpassive}}$ [mV _{MME}]	565	566	310	316
i_{Flade} [μA cm ⁻²]	1.47	0.78	83.03	8.93
$i_{\text{pass at 0 V}_{\text{MME}}}$ [μA cm ⁻²]	0.27	0.24	2.25	0.43

Hydrogen permeability experiments

The permeation transients for the tested materials were analyzed using the framework presented in the experimental part. The effective hydrogen diffusion coefficients (D_{eff}) are presented in Figure 5. Figure 6 shows the hydrogen concentrations in lattice and reversible sites (C_{OR}), and Figure 7 shows the steady state thickness normalized hydrogen fluxes ($J_{\text{ss}} L$) for the tested samples. For each sample at a given temperature, each value is the average of the three permeation transients. The error bars represent the standard deviations in the results. D_{eff} decreased, and C_{OR} increased, with increasing Ni content. There was a weak trend towards increasing $J_{\text{ss}} L$ with increasing Ni content.

C_0 , calculated from Equation (1), ranged from approximately $5 \cdot 10^{-5}$ to $5 \cdot 10^{-4}$ ppm (wt) from 15 to 70 °C. The trend with regards to Ni content was the same as for J_{ss} L shown in Figure 7.

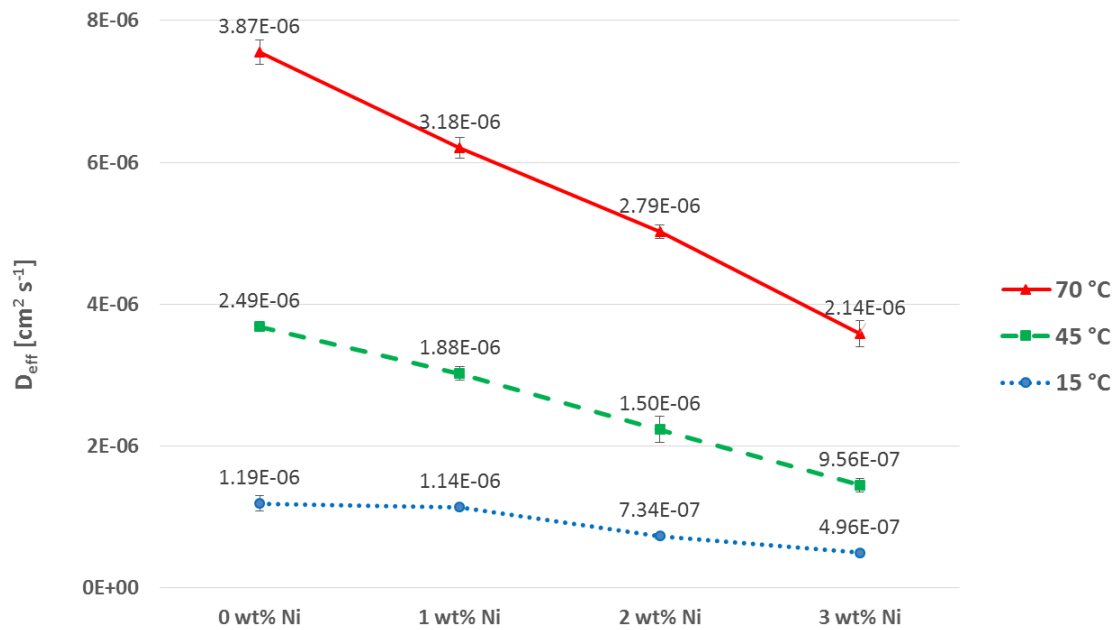


Figure 5. Effective hydrogen diffusion coefficients calculated by the t_{lag} method. The bullets are average of three permeation transients. Error bars show the standard deviations. Lines added to aid visualization.

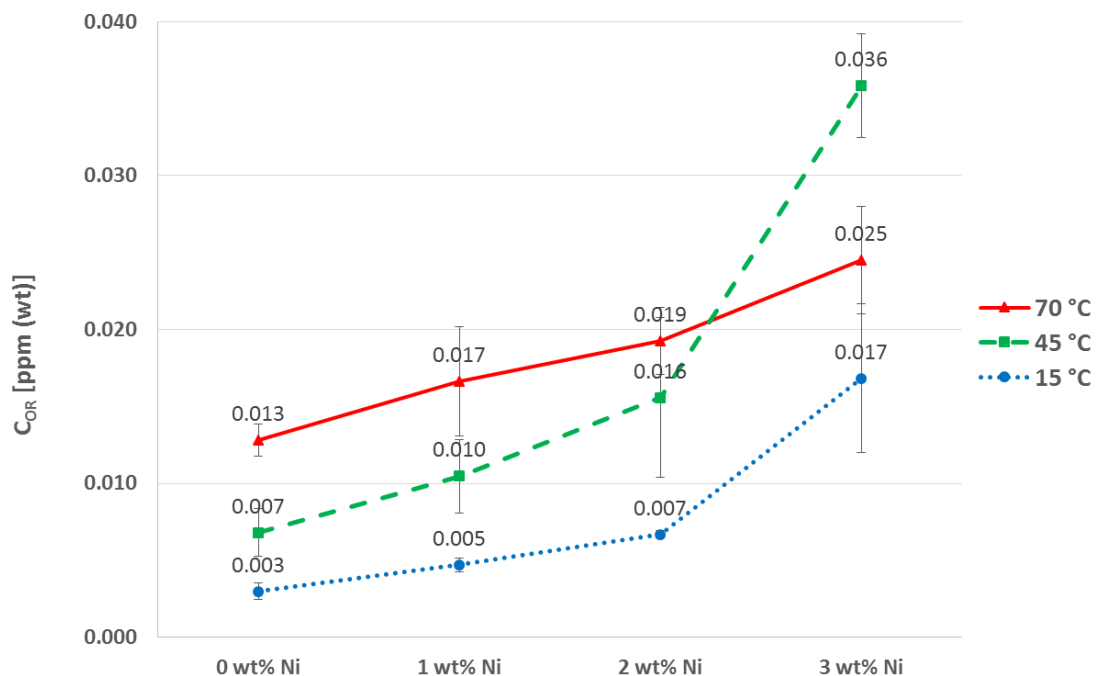


Figure 6. Hydrogen concentrations in lattice and trap sites. The bullets are average of three permeation transients. Error bars show the standard deviations. Lines added to aid visualization.

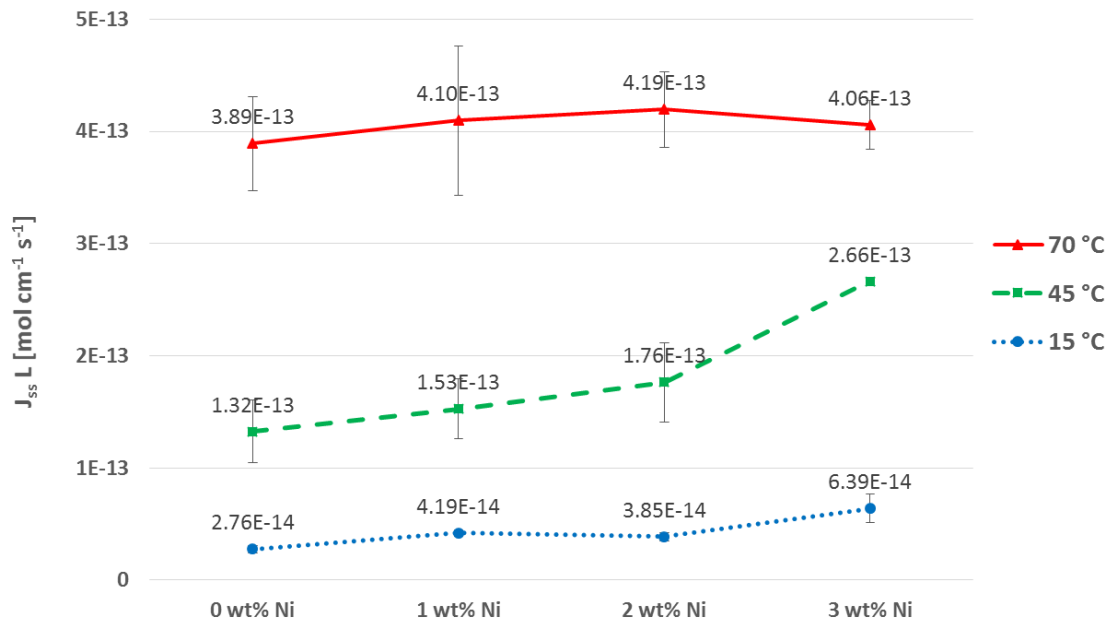


Figure 7. Thickness normalized steady-state hydrogen permeation fluxes. The bullets are average of three permeation transients. Error bars show the standard deviations. Lines added to aid visualization.

With 36 permeation transients conducted in total, it is not practical to present them all graphically. As recommended in ASTM G-148 [17], a representative sample and temperature was chosen to describe the transients. Figure 8 shows the permeation transients for the 3 wt% Ni sample at 45 °C plotted as steady-state normalized permeation flux vs. the logarithm of normalized time. The time is normalized to the sample thickness (L) and to the bcc lattice diffusion coefficient (D_l). Ideal bcc lattice diffusion, calculated from the solution of Fick's law given in ISO 17081 [16], is plotted for comparison.

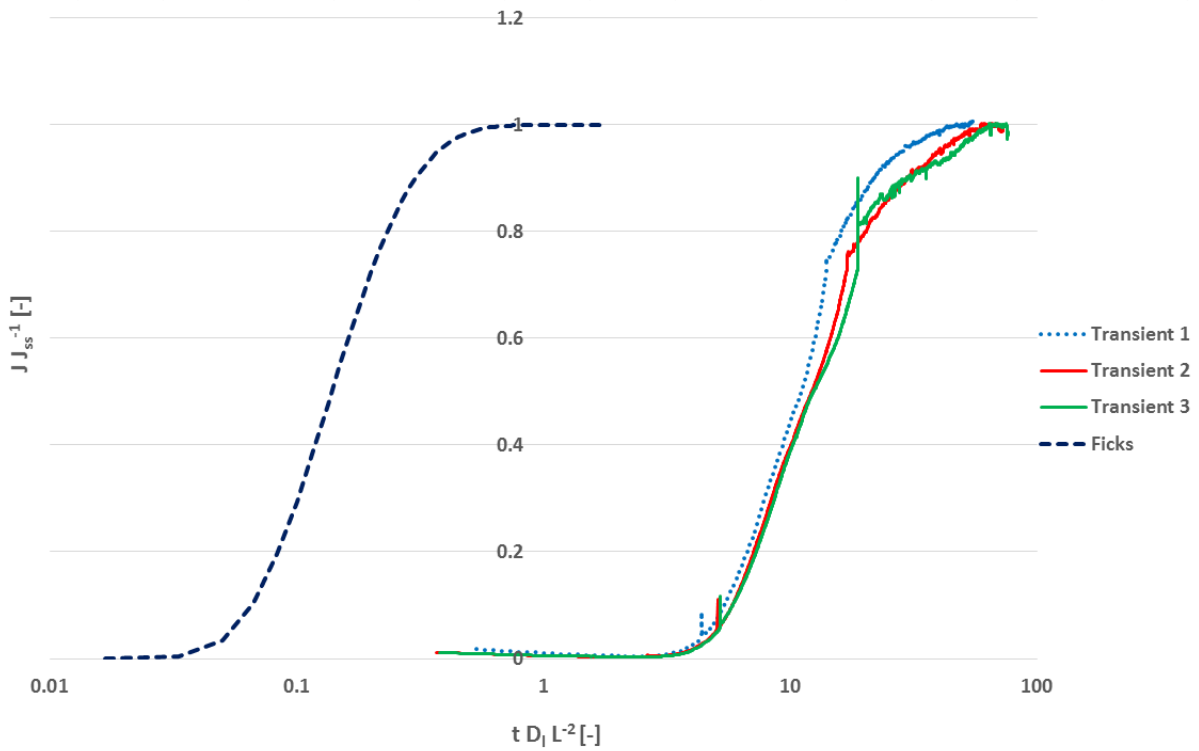


Figure 8. Permeation transients for 3 wt% Ni sample at 45 °C plotted as steady-state normalized permeation flux vs. the logarithm of normalized time. Ideal bcc lattice diffusion is plotted for comparison and is labeled “Ficks”.

A challenge sometimes encountered in the permeability experiments was that the permeation current would continue to rise instead of stabilizing at a steady-state value. This is illustrated by the difference between the third permeation transients for 0 and 1 wt% Ni samples at 45 °C, Figure 9.

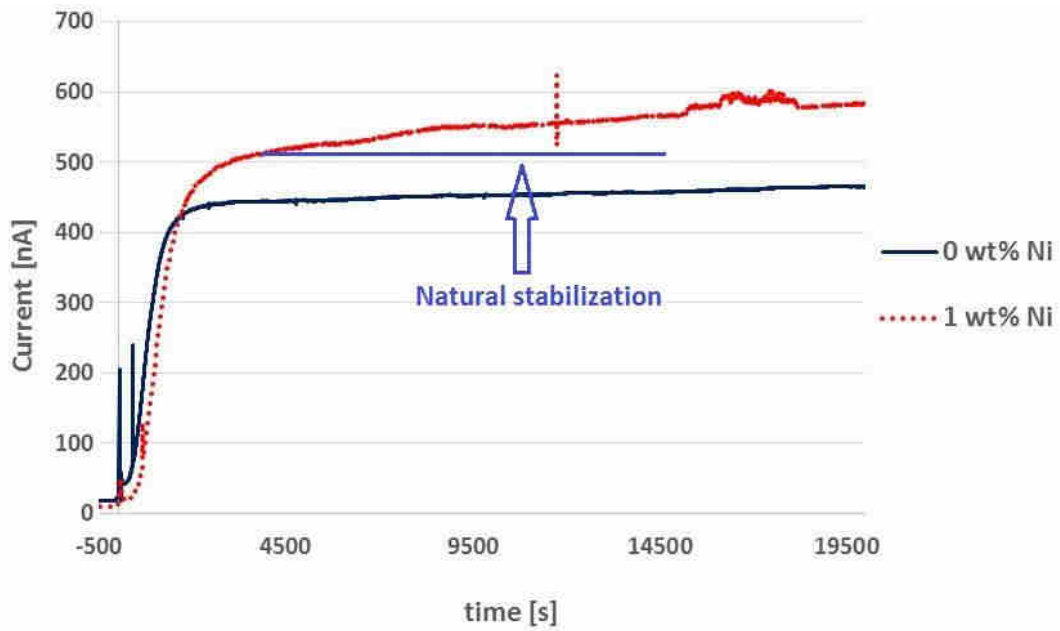


Figure 9. Permeation current vs. time for 0 and 1 wt% Ni samples at 45 °C. Both are the third charging transient at that temperature. The blue line shows the expected steady-state current stabilization that was not achieved for the 1 wt% Ni sample in this case.

Figure 10 shows the potentials on the cathodic side during the two charging transients in Figure 9. The potentials on the cathodic side during galvanostatic charging were not stable, but had a similar development with time.

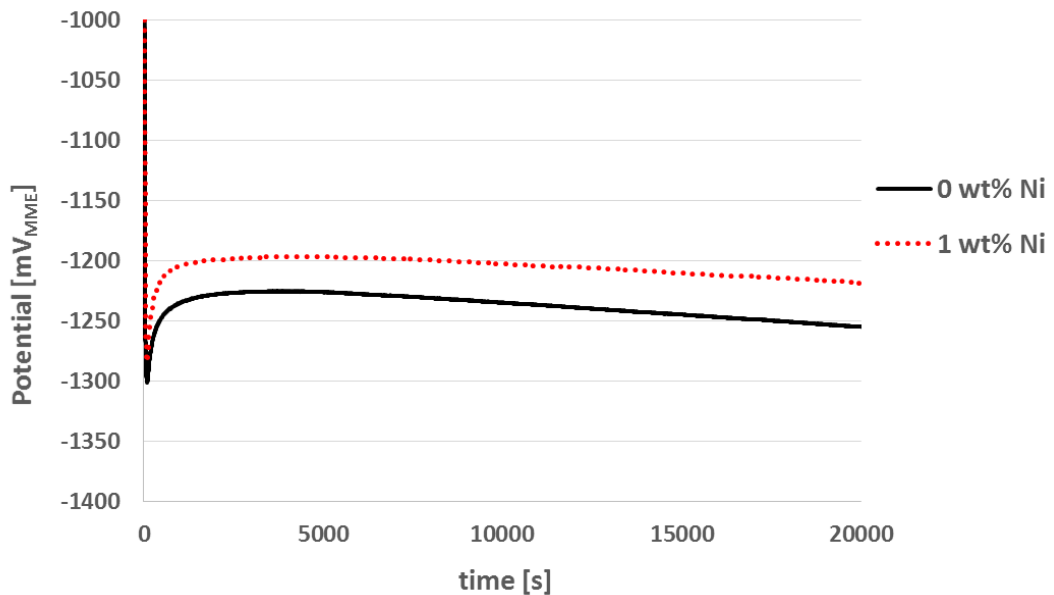


Figure 10. Potentials on cathodic side during the third hydrogen charging transients at 45 °C for 0 and 1 wt% Ni samples.

Discussion

Material characterization

As seen from the SEM micrographs in Figure 3, all samples had ferritic/pearlitic microstructures. The effect of Ni on refining ferrite grain size and morphology in low alloy steels is clear when comparing samples 0 to 1 wt% Ni and 2 to 3 wt% Ni.

The amount of pearlite appeared to increase with increasing Ni content. The 0 wt% Ni sample was somewhat oxidized during homogenization due to cracking of the quartz glass and might have become slightly decarburized. Still, the fraction of pearlite appears to increase with increasing Ni content for the other three samples. This can be explained by physical metallurgy. Because Ni is an austenite stabilizing element, it expands the austenite region in the phase diagram [27]. Ni also lowers the eutectoid temperature and reduces the carbon content of the eutectoid composition as described in [27]. The lever rule suggests that the amount of pearlite increases at the expense of ferrite for increased Ni contents.

Electrochemical polarization curves

A potential of 0 V_{MME} was chosen as the oxidation potential at the anode side in the permeability experiments because it was in the middle of the passive potential range and sufficiently anodic for hydrogen oxidation.

During cathodic polarizations, hydrogen bubbles were visually observed at current densities around 150 $\mu\text{A cm}^{-2}$ at 15 °C and around 50 $\mu\text{A cm}^{-2}$ at 70 °C. A hydrogen charging current density of 45 $\mu\text{A cm}^{-2}$ was chosen for all permeability experiments. The choice of cathodic current density, below what would give hydrogen bubbles on the surface, was with the assumption that this would provide as stable conditions as possible on the cathodic side, hence maintaining a constant sub-surface hydrogen concentration.

Hydrogen permeability experiments

Effect of nickel in solid solution

The effective diffusion coefficient decreased with increasing Ni content as seen in Figure 5. The variations between the consecutive transients, indicated by the standard deviations, were much smaller than the variations between Ni contents. The trend was independent of temperature. The magnitude of D_{eff} in the literature ranges from 10^{-7} to 10^{-4} , and direct comparison is not straightforward since D_{eff} depends on hydrogen charging conditions. In this work, D_{eff} decreased by 58, 61 and 45% from 0 to 3 wt% Ni at temperatures of 15, 45 and 70 °C, respectively.

Figure 7 showed the thickness normalized steady-state permeation fluxes ($J_{\text{ss}} L$) through the materials. As indicated by the standard deviations, $J_{\text{ss}} L$ varied somewhat between consecutive

charging transients. There was a weak trend towards increasing $J_{ss} L$ with increasing Ni content. As described in the literature [20], the steady-state permeation flux should be independent on trapping. Although the charging current density was the same on all samples, the surface coverage of H_{ads} could be different due to the effect of Ni on the catalytic properties of the surfaces. The reason for the occasional rising in steady-state permeation current, discussed later, might also be a part of the explanation.

The hydrogen concentrations in lattice and trap sites in the samples were presented in Figure 6. Even though some of the standard deviations were of similar magnitude as the difference between Ni contents, the trend was clear to increasing hydrogen solubility with increasing Ni content. Since the values were calculated by Equation (3), the trend is mostly a result of the decreasing effective diffusion coefficients with increasing Ni content. The limitations of this approach are that it considers reversible trapping only, and that trap occupancy is low. As discussed below, there was no irreversible trapping in the alloys. The trap occupancy should be low, given the low sub-surface lattice hydrogen concentrations (C_0) [20]. However, it was found by analyzing the shape of the permeation transients, discussed below, that trapping probably affected the transients to some degree. A strange result was seen for the 3 wt% Ni sample where the hydrogen solubility was higher at 45 °C than at 70 °C. For some reason, most likely experimental error, the steady-state flux of hydrogen was quite high for the 3 wt% Ni sample at 45 °C compared to the other samples at 45 °C as seen in Figure 7.

No differences were found between the first and subsequent transients at the same temperature, as exemplified in Figure 8. Since the same samples were used at all three temperatures, all irreversible traps could have been filled after the first transients at 15 °C, but no differences were seen between the first and subsequent transients at 15 °C either. According to Turnbull et al. [20], it is unlikely that irreversible traps can be neglected in steels. The same author observed a clear displacement to shorter times from the first to the second and third permeation transients, when testing a martensitic stainless steel. Other authors have failed to observe this time shift. Bolzoni et al. [28] tested two pipeline steel materials (X65 and F22) in as received conditions, fully quenched and annealed conditions, and found no differences between permeation transients. Chan [29] reported permeability tests on a martensitic steel with various carbon contents. As the carbon content increased, quenching produced more lattice imperfections that acted as irreversible traps. The difference between the first and second permeation transients increased as the carbon content increased from 0.23 to 0.93 wt%. Chan suggested that microcracks, microvoids, and retained austenite were irreversible traps in his steels.

When the time was normalized to D_{eff} instead of D_l (as in Figure 8), the experimental permeation curves in the normalized plot matched the curve for ideal lattice diffusion at $J J_{ss}^{-1} = 0.63$, and the shape of the permeation transients could easily be compared with the curve for ideal lattice diffusion. If experimental curves are steeper than that of ideal lattice diffusion, it may indicate that trap occupancy is significant. If permeation transients are less steep than the ideal lattice diffusion curve, it may indicate unsteady surface conditions [17]. The majority of the 36 permeation transients were slightly steeper than the ideal lattice diffusion curve, several of the curves had the same steepness, and a few curves were less steep.

Trap number and energies were estimated using Equations (5) - (8). The number of traps ranged from $9.89 \cdot 10^{22}$ to $6.27 \cdot 10^{23}$ sites cm^{-3} . The trap energies ranged from 9.2 kJ mol^{-1} to 15.4 kJ

mol^{-1} . Both the number of reversible traps, the trap energy, and the total trapping energy (number of traps multiplied with trap energy) varied without a clear trend between Ni contents. The result was the same if using data only from 15 to 45 °C or from 45 to 70 °C. The reason for the lack of correlation is unknown and remains the scope of ongoing research activities.

Experimental challenges

As seen in Figure 9, the permeation current would sometimes continue to increase with time instead of stabilizing. Among the 35 permeation transients recorded, 17 had fairly well-defined steady-state currents, while 18 displayed a monotonous increase in permeation currents. The rise in permeation current was encountered more often at 15 °C than at 70 °C. The probable explanation is unsteady surface conditions on the cathode side. When switching to anodic potential after OCP before the first permeation transients, the current densities decreased with time. As seen in Figure 4, the material exhibited an active-passive behavior in the electrolyte. How the material obtains passivity was not investigated, but there is indeed a time-dependent alteration of the surface. The cathodic side shifted between anodic and cathodic potential, and it is likely that the surface conditions on the cathodic side changed with time after switching to cathodic potentials.

The changes in potential on the cathodic side with time during hydrogen charging, seen in Figure 10, support that the surface conditions were not stable. However, the cathodic potentials appeared the same for the permeation transients that stabilized and those where the current continued to increase. As seen in Figure 10, the cathodic potentials had close to identical courses with time even though the anodic permeation transients, seen in Figure 9, were quite different. In Figure 10, the cathodic potential was lower for the 0 wt% Ni sample than for the 1 wt% Ni sample at the same charging current. This varied from transient to transient at the same material, and there was no overall trend towards a Ni content having a higher or lower potential during galvanostatic charging.

Challenges with unsteady surface conditions on the hydrogen charging side have been reported previously by Zakroczyński [30], who investigated the permeability of iron by cathodically generating hydrogen in a 0.1 M NaOH solution. In this case, a barrier layer formed on the surface at OCP, which hampered the entry of hydrogen into iron after switching to cathodic charging. During cathodic charging, the film was gradually removed by a reduction process [30] (although probably never completely removed [31]). It was shown using ellipsometry that the surface layer changed with time during cathodic charging [31]. The result was that the permeation current on the anodic side continued to increase for up to 50 h before a constant flux was obtained. Casanova and Crousier [32] suggested that such changes can be related either to the diffusion coefficient of the surface layer, or to the surface coverage of adsorbed hydrogen.

When calculating D_{eff} , C_{OR} and $J_{\text{ss}} L$, steady-state was selected where it was expected to stabilize as indicated in Figure 9. The curves with normalized permeation flux vs. logarithm of normalized time then had shapes similar to the ideal diffusion curve (only delayed in time) as seen in Figure 8. When J_{ss} was selected at the end of the charging period, the curves had ideal appearance up to some point, before the slope would change the last part up to $J J_{\text{ss}}^{-1}$ equal to one. Despite the probable error when using the current at the end of the transients (regardless

of curve shape) to calculate D_{eff} and C_{OR} , the relations with regards to Ni content were the same: D_{eff} decreased, and C_{OR} increased, with increasing Ni content.

When comparing the permeation current in Figure 9 to the passive current densities from the polarization curves, given in Table 2, they appear as of similar magnitude. This was not the case as the background passive current decreased with time before the charging transients started in the permeability experiments. While the background current for the transients in Figure 9 was about 10 nA, the steady-state permeation current was higher than 400 nA.

Effect of microstructure

As already discussed, Ni refined the microstructure and increased the pearlite fraction. Several investigators have found that the amount, location, and morphology of cementite affects hydrogen diffusion and solubility within steels [33-36]. Chan and Charles [33] found that with increasing carbon content in a ferritic/pearlitic steel, the hydrogen solubility increased, and the effective diffusion coefficient decreased. Similarly, a reduced grain size has been found to increase hydrogen pick-up in pure iron [37].

Using data from literature to remove the effects of varying pearlite contents and grain sizes in the current results is difficult. One of the problems is the hydrogen concentration dependency of D_{eff} . Additional investigations should be done with variations in grain sizes and, if possible, decarburized samples to confirm that the trend found in this work is indeed the effect of Ni in solid solution, and not an effect of cementite content or grain size variations.

Implication of the results

The relation between experimental results such as D_{eff} and C_{OR} and the materials resistance to HSC is not fully understood. Diffusible hydrogen enhances crack propagation, and threshold concentrations of hydrogen can be defined [38]. Similarly, HSC susceptibility generally increases with increasing hydrogen diffusion rates [39].

For a given steel in different environments, good correlation has been found between increased thickness normalized steady-state permeation flux and reduced cracking resistance [40]. However, this simply means that a more severe environment enhances the risk of cracking, and does not provide a criterion to compare and evaluate different alloys or microstructures.

As stated by Koh et al. [39], SSC results from the combined action of hydrogen and metallurgical defects that are sensitive to hydrogen embrittlement. If an added microstructural characteristic is a critical crack initiation point in itself, the susceptibility to HSC may increase even if both D_{eff} and C_{OR} decrease. If nickel, in this case, is not a crack initiation point in itself, reduced D_{eff} and C_{OR} values are desired. When D_{eff} decreases while C_{OR} increases, the effect on in-service cracking resistance is not apparent. Fracture testing could provide additional information on the effect of Ni in solid solution on the HSC susceptibility of the ferrite phase.

Conclusions

Electrochemical hydrogen permeability experiments were used to investigate the effect of solid solution nickel (Ni) on hydrogen diffusion, solubility, and trapping in steels. Ferritic/pearlitic research grade low alloy steels with nominal Ni contents from 0 to 3 wt% were tested at 15, 45 and 70 °C with three permeation transients at each temperature.

The following conclusions were made based on the results presented herein:

- The effective diffusion coefficient decreased, and the hydrogen solubility in lattice and reversible sites increased, with increasing Ni content at all tested temperatures.
- Irreversible trapping was not found in any of the tested samples as evidenced by the negligible difference between the first and the subsequent permeation transients.
- The effect of Ni on the microstructure might be superimposed the effect of Ni in solid solution. This should be investigated in further work.

Acknowledgements

This work is part of an international cooperation agreement between Norwegian University of Science and Technology (NTNU), General Electric (GE), Tenaris, YPF-Technología, and the Universidad Nacional de San Martín/Comisión Nacional de Energía Atómica (UNSAM/CNEA). The work was financed by NTNU and GE.

References

- [1] ISO 15156-2 Petroleum and natural gas industries - Materials for use in H₂S-containing environments in oil and gas production -- Part 2: Cracking-resistant carbon and low-alloy steels, and the use of cast irons, International Organization for Standardization, Geneva, Switzerland (2015).
- [2] M. Kappes, M. Iannuzzi, R. B. Rebak, and R. M. Carranza, "Sulfide stress cracking of nickel-containing low-alloy steels," in *Corrosion Reviews* vol. 32, ed, 2014, p. 101.
- [3] S. D. Cramer and B. S. Covino, Jr., "ASM Handbook, Volume 13A - Corrosion: Fundamentals, Testing, and Protection," ed: ASM International, pp. 367-374.
- [4] Y. Yoshino and Y. Minozaki, "Sulfide stress cracking resistance of low-alloy nickel steels," *Corrosion*, vol. 42, pp. 222-233, 1986.
- [5] H. Asahi and M. Ueno, "Effects of Ni Addition on Sulfide Stress Cracking Resistance of Low Alloy Tempered Martensite Steels," *ISIJ international*, vol. 34, pp. 290-294, 1994.
- [6] Y. Yamane, "Effect of Ni on sulfide stress corrosion cracking in low alloy steels," Y. Yamane, et al., *Iron & Steel Research Laboratories, Kawasaki Steel Corp., 1 Kawasaki-cho, Chiba, Japan, Corrosion 86/167, NACE, Houston, TX, 1987.*
- [7] B. Wilde, C. Kim, and J. Turn Jr, "The influence of noble metal additions on the sulfide corrosion performance of AISI 4130 steel," *Corrosion*, vol. 38, pp. 515-524, 1982.

- [8] W. Beck, J. Bockris, M. Genshaw, and P. Subramanyan, "Diffusivity and solubility of hydrogen as a function of composition in Fe-Ni alloys," *Metallurgical Transactions*, vol. 2, pp. 883-888, 1971.
- [9] W. Dresler and M. Froberg, "Diffusion Coefficient of H in the System Fe-Ni at 25 and 58 C," *J. Iron Steel Inst.*, vol. 211, pp. 298-302, 1973.
- [10] Y. Yamanishi, T. Tanabe, and S. Imoto, "Hydrogen Permeation and Diffusion through Pure Fe, Pure Ni and Fe-Ni Alloys," *Transactions of the Japan institute of metals*, vol. 24, pp. 49-58, 1983.
- [11] W. T. Becker and R. J. Shipley, "ASM Handbook, Volume 11 - Failure Analysis and Prevention," ed: ASM International, pp. 691-693.
- [12] M. Kohno, M. Makioka, S. Kinoshita, and A. Suzuki, "Mechanical Properties of Vacuum Carbon-Deoxidized Thick-Wall 21/4Cr-1Mo Steel Forging," in *STP 755-EB - Application of 2 1/4Cr-1 Mo Steel for Thick-Wall Pressure Vessels*. vol. STP 755-EB, G. Sangdahl and M. Semchyshen, Eds., ed West Conshohocken, PA: ASTM International, 1982, pp. 208-227.
- [13] ASTM E1019-11 Standard Test Methods for Determination of Carbon, Sulfur, Nitrogen, and Oxygen in Steel, Iron, Nickel, and Cobalt Alloys by Various Combustion and Fusion Techniques, ASTM International, West Conshohocken (2011).
- [14] ASTM E1479-99 Standard Practice for Describing and Specifying Inductively-Coupled Plasma Atomic Emission Spectrometers, ASTM International, (2011).
- [15] M. A. Razzak, "Heat treatment and effects of Cr and Ni in low alloy steel," *Bulletin of Materials Science*, vol. 34, pp. 1439-1445, 2011.
- [16] ISO 17081:2014 Method of measurement of hydrogen permeation and determination of hydrogen uptake and transport in metals by an electrochemical technique, International Organization for Standardization, Geneva, Switzerland (2014).
- [17] ASTM G148-97 Standard Practice for Evaluation of Hydrogen Uptake, Permeation, and Transport in Metals by an Electrochemical Technique, ASTM International,, West Conshohocken, PA (2011).
- [18] C. Hamann, A. Hamnett, and W. Vielstich, "Electrochemistry, 2nd completely revised and updated ed," ed: Weinheim: Wiley-VCH Pub, 2007, pp. 98-102.
- [19] A. Turnbull, "4 - Hydrogen diffusion and trapping in metals A2 - Gangloff, Richard P," in *Gaseous Hydrogen Embrittlement of Materials in Energy Technologies*. vol. 1, B. P. Somerday, Ed., ed: Woodhead Publishing, 2012, pp. 89-128.
- [20] A. Turnbull, M. W. Carroll, and D. H. Ferriss, "Analysis of hydrogen diffusion and trapping in a 13% chromium martensitic stainless steel," *Acta Metallurgica*, vol. 37, pp. 2039-2046, 7// 1989.
- [21] A. Turnbull and M. W. Carroll, "The effect of temperature and H₂S concentration on hydrogen diffusion and trapping in a 13% chromium martensitic stainless steel in acidified NaCl," *Corrosion Science*, vol. 30, pp. 667-679, // 1990.
- [22] A. Turnbull and G. Hinds, "*Hydrogen Diffusion in Corrosion Resistant Alloys*", CORROSION 2004, 2004/1/1/ (2004).
- [23] V. Olden, A. S. Hauge, and O. M. Akselsen, "*The Influence of Plastic Strain On the Effective Hydrogen Diffusion Coefficient And Trapping In Base Metal And Weld Simulated Heat Affected Zone of an X70 Pipeline Steel*", The Twenty-second International Offshore and Polar Engineering Conference, 2012/1/1/ (2012).
- [24] M. Skjellerudsveen, O. M. Akselsen, V. Olden, R. Johnsen, and A. Smirnova, "Effect of Microstructure and Temperature on Hydrogen Diffusion and Trapping in X70 grade Pipeline Steel and its Weldments," in *EuroCorr 2010, Moskva*, 2010.
- [25] A. J. Griffiths and A. Turnbull, "On the effective diffusivity of hydrogen in low alloy steels," *Corrosion Science*, vol. 37, pp. 1879-1881, 11// 1995.

- [26] A. Turnbull, "Perspectives on hydrogen uptake, diffusion and trapping," *International Journal of Hydrogen Energy*, vol. 40, pp. 16961-16970, 12/21/ 2015.
- [27] G. Krauss, "Steels - Processing, Structure, and Performance (2nd Edition)," ed: ASM International, pp. 17-38.
- [28] F. Bolzoni, G. Re, M. Ormellese, E. Fallahmohammadi, G. Fumagalli, and L. Lazzari, "Electrochemical Investigation of Hydrogen Diffusion in Pipeline Steels," *Corrosion/2013, paper*, 2013/3/17/ 2013.
- [29] S. L. I. Chan, "Hydrogen trapping ability of steels with different microstructures," *Journal of the Chinese Institute of Engineers*, vol. 22, pp. 43-53, 1999.
- [30] T. Zakroczymski, "Permeability of iron to hydrogen cathodically generated in 0.1 M NaOH," *Scripta Metallurgica*, vol. 19, pp. 521-524, 1985.
- [31] T. Zakroczymski, Z. Szklarska-Smialowska, and T. Zakroczymski, "Activation of the Iron Surface to Hydrogen Absorption Resulting From a Long Cathodic Treatment in NaOH Solution," *J. Electrochem. Soc*, vol. 132, pp. 2548-2552, 1985.
- [32] T. Casanova and J. Crousier, "The influence of an oxide layer on hydrogen permeation through steel," *Corrosion Science*, vol. 38, pp. 1535-1544, 1996/09/01 1996.
- [33] S. Chan and J. Charles, "Effect of carbon content on hydrogen occlusivity and embrittlement of ferrite-pearlite steels," *Materials science and technology*, vol. 2, pp. 956-962, 1986.
- [34] H. W. Jeng, L. H. Chiu, D. L. Johnson, and J. K. Wu, "Effect of pearlite morphology on hydrogen permeation, diffusion, and solubility in carbon steels," *Metallurgical Transactions A*, vol. 21, pp. 3257-3259, 1990/12/01 1990.
- [35] H.-L. Lee and S. Lap-Ip Chan, "Hydrogen embrittlement of AISI 4130 steel with an alternate ferrite/pearlite banded structure," *Materials Science and Engineering: A*, vol. 142, pp. 193-201, 8/30/ 1991.
- [36] W. C. Luu and J. K. Wu, "The influence of microstructure on hydrogen transport in carbon steels," *Corrosion Science*, vol. 38, pp. 239-245, 2// 1996.
- [37] M. Martinez-Madrid, S. Chan, and J. Charles, "Hydrogen occlusivity and embrittlement in iron-effect of grain structure and cold work," *Materials Science and Technology*, vol. 1, pp. 454-460, 1985.
- [38] G. T. Park, S. U. Koh, H. G. Jung, and K. Y. Kim, "Effect of microstructure on the hydrogen trapping efficiency and hydrogen induced cracking of linepipe steel," *Corrosion Science*, vol. 50, pp. 1865-1871, 7// 2008.
- [39] S. U. Koh, J. S. Kim, B. Y. Yang, and K. Y. Kim, "Effect of Line Pipe Steel Microstructure on Susceptibility to Sulfide Stress Cracking," *Corrosion*, vol. 60, pp. 244-253, 2004/3/1/.
- [40] M. S. de Santa Maria and A. Turnbull, "The effect of H₂S concentration and pH on the cracking resistance of AISI 410 stainless steel in 5% brine," *Corrosion science*, vol. 29, pp. 69-88, 1989.